

## MARTIAN GEOLOGY

# Large wind ripples on Mars: A record of atmospheric evolution

M. G. A. Lapotre,<sup>1\*</sup> R. C. Ewing,<sup>2</sup> M. P. Lamb,<sup>1</sup> W. W. Fischer,<sup>1</sup> J. P. Grotzinger,<sup>1</sup> D. M. Rubin,<sup>3</sup> K. W. Lewis,<sup>4</sup> M. J. Ballard,<sup>2</sup> M. Day,<sup>5</sup> S. Gupta,<sup>6</sup> S. G. Banham,<sup>6</sup> N. T. Bridges,<sup>7</sup> D. J. Des Marais,<sup>8</sup> A. A. Fraeman,<sup>1,9</sup> J. A. Grant,<sup>10</sup> K. E. Herkenhoff,<sup>11</sup> D. W. Ming,<sup>12</sup> M. A. Mischna,<sup>9</sup> M. S. Rice,<sup>13</sup> D. A. Sumner,<sup>14</sup> A. R. Vasavada,<sup>9</sup> R. A. Yingst<sup>15</sup>

Wind blowing over sand on Earth produces decimeter-wavelength ripples and hundred-meter-to kilometer-wavelength dunes: bedforms of two distinct size modes. Observations from the Mars Science Laboratory Curiosity rover and the Mars Reconnaissance Orbiter reveal that Mars hosts a third stable wind-driven bedform, with meter-scale wavelengths. These bedforms are spatially uniform in size and typically have asymmetric profiles with angle-of-repose lee slopes and sinuous crest lines, making them unlike terrestrial wind ripples. Rather, these structures resemble fluid-drag ripples, which on Earth include water-worked current ripples, but on Mars instead form by wind because of the higher kinematic viscosity of the low-density atmosphere. A reevaluation of the wind-deposited strata in the Burns formation (about 3.7 billion years old or younger) identifies potential wind-drag ripple stratification formed under a thin atmosphere.

**B**edforms are repeating topographic forms on a granular surface that arise because of interactions between the sediment bed, sediment transport, and fluid flow (1). Bedforms typically manifest as ripples or dunes made of sand mobilized by air or water. They create spatial patterns that are recognizable on the surfaces of Venus, Earth, Mars, Titan, and comet 67P (2, 3) and leave stratified sedimentary deposits. Because their morphology depends on

formation mechanisms (4–6), bedforms are a primary means to reconstruct active and ancient atmospheric and hydrologic conditions.

Wind-driven (eolian) bedforms on Earth display two distinct scales: decimeter-wavelength sand ripples and hundred-meter- to kilometer-wavelength dunes (4, 7) (Fig. 1A). Grain-impact processes are thought to dominate the formation of wind ripples, whereas dune formation involves an aerodynamic instability (6). Orbital observations of

Mars also show the superposition of two distinct scales of active bedforms (Fig. 1B and fig. S3) (8). Martian dunes form at a similar wavelength as on Earth; however, those dunes are ubiquitously mantled with bedforms 1 to 5 m in wavelength (hereafter referred to as large martian ripples) (9).

Large martian ripples were thought to have a similar origin to decimeter-wavelength eolian impact ripples on Earth, but to be larger on Mars because of differences in saltation (ballistic hopping of grains) (6). An implicit assumption under this hypothesis is that small wind ripples should not coexist with large martian ripples. Until recently, the spatial coexistence of three scales of bedforms could not be tested because the resolution of orbital imagery was too coarse [25 to 50 cm per pixel in

<sup>1</sup>Division of Geological and Planetary Science, California Institute of Technology, Pasadena, CA 91125, USA.

<sup>2</sup>Department of Geology and Geophysics, Texas A&M University, College Station, TX 77843, USA. <sup>3</sup>Department of Earth and Planetary Sciences, University of California Santa Cruz, Santa Cruz, CA 95064, USA. <sup>4</sup>Department of Earth and Planetary Sciences, Johns Hopkins University, Baltimore, MD 21218, USA. <sup>5</sup>Jackson School of Geosciences, University of Texas at Austin, Austin, TX 78712, USA. <sup>6</sup>Department of Earth Science and Engineering, Imperial College London, London SW7 2AZ, UK. <sup>7</sup>Applied Physics Laboratory, Johns Hopkins University, Laurel, MD 20723, USA. <sup>8</sup>NASA Ames Research Center, Moffett Field, CA 94035, USA. <sup>9</sup>Jet Propulsion Laboratory, California Institute of Technology, Pasadena, CA 91109, USA. <sup>10</sup>National Air and Space Museum, Smithsonian Institution, Washington, DC 20560, USA. <sup>11</sup>Astrogeology Science Center, U.S. Geological Survey, Flagstaff, AZ 86001-1698, USA. <sup>12</sup>NASA Johnson Space Center, Houston, TX 77058, USA. <sup>13</sup>Geology Department, Western Washington University, Bellingham, WA 98225-9080, USA. <sup>14</sup>Department of Earth and Planetary Sciences, University of California, Davis, CA 95616, USA. <sup>15</sup>Planetary Science Institute, Tucson, AZ 85719, USA.

\*Corresponding author. Email: mlapotre@caltech.edu

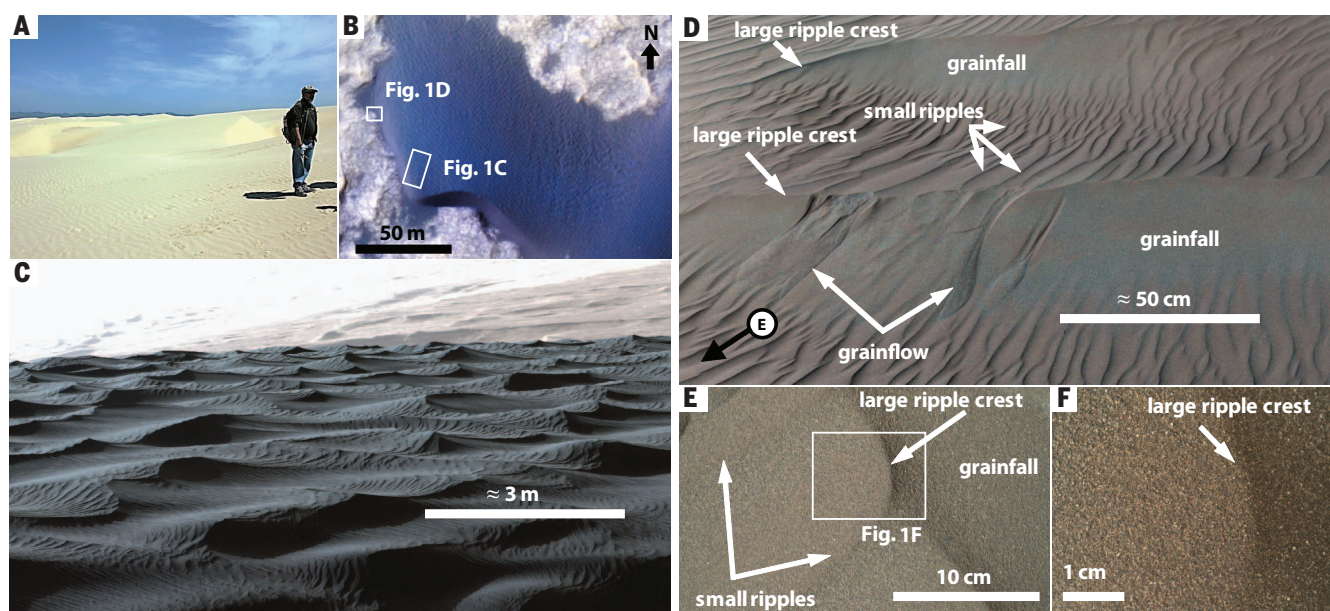


**Fig. 1. Eolian bedforms on Earth and Mars.** (A) Dunes and ripples at Oceano Dunes, California, United States (35.094960°N, -120.623476°E). (B) to (F) Dune in the Bagnold dune field, Gale crater, Mars, as shown from (B) a HiRISE image (ESP\_035917\_1755) and [(C) to (F)] the Curiosity rover. (C) Mastcam mosaic (mcam05410, sol 1192) showing small and large ripples on the dune. (D) Mastcam image (mcam05600, sol 1221) of large ripples with superimposed small ripples. (E) MAHLI 25-cm standoff image (1223MH0005550010403094C00, sol 1223), ~1 m off frame of (D) in the direction of the black circle and arrow. (F) 5-cm standoff image (1223MH0005560010403097C00, sol 1223) of the crest of a large ripple.

High Resolution Imaging Experiment (HiRISE) images (10)] to detect decimeter-scale ripples, and rovers had not visited active dune fields, only sand sheets and coarse-grained ripples (11, 12, 13). Observations made by the Curiosity rover (14) at an active dune field (the Bagnold dune field) (15) in Gale crater now show that large martian ripples are not simply larger versions of the decimeter-scale wind ripples seen on Earth. Rather, we observe decimeter-scale ripples superimposed on larger, meter-scale ripples, which are in turn superimposed on dunes (Fig. 1 and fig. S2). Thus, two stable ripple-scale bedforms coexist on Mars and both are superimposed on dunes, in contrast to the single scale of superimposed terrestrial ripples.

Mast Camera [Mastcam (14)] images collected by Curiosity indicate that large martian ripples have morphologies unlike those of eolian impact ripples. Terrestrial impact ripples have straight crestlines created by lateral grain splash (16), and relatively subdued profiles (17). In contrast, the large ripples of the Bagnold dune field have sinuous crest lines and asymmetric topographic profiles with distinct upwind (stoss) and downwind (lee) slope angles. Furthermore, the stoss slopes of the large ripples are mantled by small-scale ripples with a wavelength range of ~5 to 12 cm, which, based on their straight crestlines, we interpret as impact ripples similar to those of Earth (Fig. 1, C and D). This interpretation is consistent with recent numerical modeling that predicts that martian impact ripples should have decimeter-scale wavelengths (18). In contrast, the crests of the large ripples are sharp and give way down-slope to angle-of-repose slip faces (slopes dipping ~30° downwind; fig. S5A) marked by the presence of grainflows [small avalanche deposits (Fig. 1D)], indicating recent activity. The presence of grain-fall (i.e., sand that settles out on the lee slope) and deflected impact ripples on the lee slope indicates the aerodynamic influence of the large ripples contemporaneous with small-ripple migration (Fig. 1D).

We compiled a comprehensive multiscale data set of eolian bedform wavelengths on Mars by combining remote measurements from 11 martian sites (fig. S1 and tables S1 and S2), with rover measurements from stereo imagery in Gale crater (fig. S5) (7). Our statistical analysis confirms that Mars has an additional bedform-wavelength mode and that meter-scale ripples are absent in terrestrial eolian landscapes (Fig. 2 and table S3) (7).

Large martian ripples are not simply small dunes, because they maintain a stable size, whereas meter-wavelength dunes, which are rare on Earth, grow as they translate downwind (6) (fig. S3 versus fig. S4). Large martian ripples mantled with impact ripples also cannot be explained as large versions of terrestrial impact ripples forming by large saltation (18, 19); no existing model can reproduce the coexistence and coevolution of two scales of impact ripples (20) (supplementary online text). Moreover, the large-ripple morphology differs significantly from that of impact ripples. An alternative interpretation of the large ripples is that they are coarse-grained ripples (21). However, images from the Mars Hand Lens Imager [MAHLI (14)] show well-

sorted large ripples up the dune's stoss slopes (Fig. 1E), with very fine to medium sand and no significant grain-size differences between the small and large ripples (Fig. 1, E and F). Thus, neither the impact nor the coarse-grained hypothesis readily explains the coexistence of two distinct equilibrium scales of active ripples composed of sediments of similar size.

Their stable size, sinuous crests, and asymmetric profiles with avalanche faces make the large martian ripples morphologically similar to terrestrial subaqueous current ripples (fig. S6), also called fluid-drag ripples (22) (supplementary text). If the large martian ripples form aerodynamically [i.e., wind-drag ripples (4, 23)], then theory developed for current ripples should predict their scale once adjusted for martian conditions. Decades of flume experiments (24, 25) have led to

scaling relations for current ripples (25, 26). Following the theoretical framework of (25), we cast ripple size data in terms of the dimensionless current ripple wavelength,  $\lambda^* = \frac{u_*}{\nu} \lambda$  [where  $\lambda$  is ripple wavelength,  $\nu$  is kinematic fluid viscosity,  $u_*$  is bed shear velocity, and  $\nu/u_*$  is proportional to the viscous sublayer thickness (25)], which is a function of the parameter  $\text{Re}_p \sqrt{\tau_*}$  [where  $\text{Re}_p$  is particle Reynolds number and  $\tau_*$  is Shields stress (fig. S7 and supplementary text)]. These dimensionless variables provide a complete description of ripple-size scaling that accounts for fluid and grain properties and for gravity. A large database of current ripple wavelengths (25), updated here to include results from high-viscosity fluids (24), illustrates that

$$\lambda^* = 2453(\text{Re}_p \sqrt{\tau_*})^{1/3} \quad (1)$$

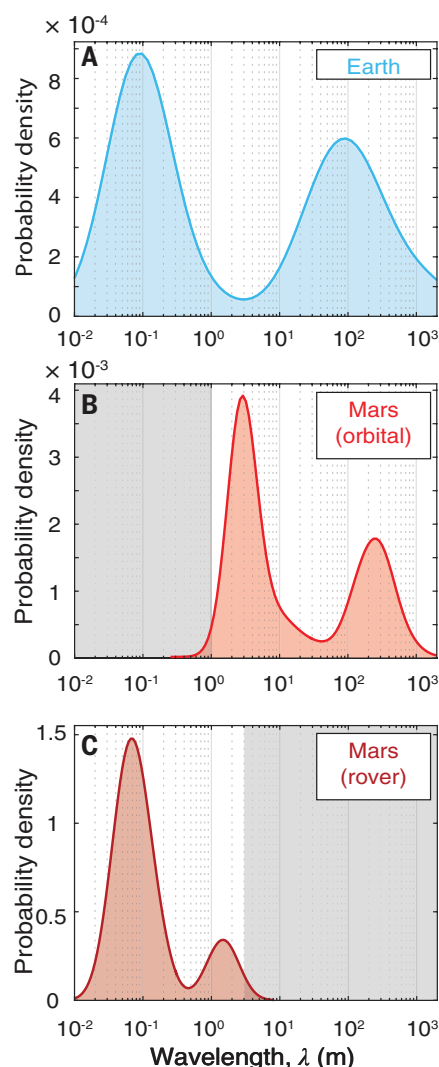


**Fig. 2. Distinct modes of eolian bedforms on Earth and Mars.** Bedform wavelength distribution on (A) Earth ( $n = 1473$  bedforms), (B) Mars from orbit ( $n = 2430$  bedforms; the shaded area is below the limit of detection), and (C) the Curiosity rover ( $n = 44$  bedforms; the shaded area is constrained by perspective from the ground) (7).

(Fig. 3). To compare the predictions of fluid-drag ripple wavelengths to the large martian ripples, we calculated  $\text{Re}_p \sqrt{\tau_*}$  and  $\lambda^*$  for all compiled martian bedforms (7) (supplementary text). Results show that wind-drag ripples on Mars are predicted to be much larger than the decimeter-scale impact ripples because of the high kinematic viscosity in Mars' low-density atmosphere; furthermore, the wavelength of the large martian ripples is consistent with fluid-drag theory (Fig. 3) across a range of elevations with different atmospheric density (fig. S10).

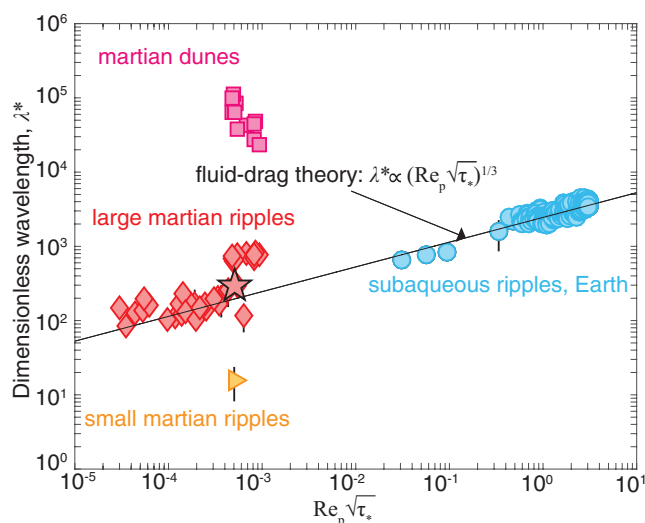
Because wind-drag ripples are predicted to be smaller in thicker atmospheres, identification of these bedforms in ancient sedimentary rocks (27) offers the potential to reconstruct atmospheric loss and the global drying of Mars (28). The migration of bedforms produces cross-stratification in sedimentary rocks, which can be used to determine their original three-dimensional geometry. Based on morphology and scale, and using a kinematic model (29) (Fig. 4), we expect sinuous wind-drag ripples formed under present-day martian atmospheric conditions (30) to form decimeter-thick trough cross-sets, grouped into larger sets formed by overall migration of the dune (supplementary text). Large-ripple stratification should be distinct from that of compound wind dunes or coarse-grained ripples, because compound dunes do not maintain a persistently stable size in the down-dip direction (fig. S3 versus fig. S4) and typically form thicker cross-sets, and coarse-grained ripples leave recognizable coarse-grained lags. Stratification from the large ripples might also resemble that of subaqueous ripples and dunes. However, identification of distinctive wind-ripple strata [inversely graded millimeter-thick continuous layers (31)] coexisting with both decimeter-scale cross-sets and meter-scale dune troughs would enable the definitive interpretation of an eolian origin, whereas other contextual support, such as fluvial bar sets, desiccation cracks, and soft-sediment deformation, would characterize wet environments (27).

Candidate wind-drag ripples were observed by the Opportunity rover at Cape St. Mary, Victoria crater, in the Burns formation (Fig. 4 and supplementary text) (32) and were recognized as



**Fig. 3. Scaling of fluid-drag ripples.**

Dimensionless bedform wavelength as a function of particle Reynolds number,  $Re_p$ , and Shields stress,  $\tau_*$ , quantities that control fluid-drag ripple size (25) (current ripples, blue circles; theory, black line). In contrast to martian dunes (pink squares) and small martian ripples (orange triangles), large martian ripples [red diamonds,  $n = 7280$  bedforms, measured over 36 locations globally, including our measurements (7) and those of (38); the red star indicates rover measurements at Gale crater] match fluid-drag ripple theory. Symbols are means and error bars represent standard deviations at a given measurement site; error bars are smaller than marker size where not shown.



abnormally sinuous and large eolian ripples at the time. There, repeated 10- to 20-cm-thick trough cross-sets are bounded by meter-scale dune troughs. The morphology, scale, contextual relationship to distinctly larger bounding surfaces, and apparent high deposition rate (32) all support the hypothesis that this stratification was formed by wind-drag ripples. The wind-drag ripple hypothesis therefore indicates a substantially thinned martian atmosphere during deposition of the Late Noachian–Early Hesperian Burns formation (fig. S10) (33). This interpretation supports models of atmospheric loss based on carbon isotope calculations (28). It is also consistent with centimeter-scale trough cross-strata in sulfate-rich sands in the lower Burns formation (27) that indicate subaqueous flows discharged from melt- or groundwater as brines of high ionic strength, rather than meteoric precipitation, due to the highly soluble sand rains (26, 34, 35). Although the relative ages are highly uncertain, our analysis suggests that ancient lakes in Gale crater (36) might predate the inferred low-density atmosphere associated with the lower Burns formation. Thus, whereas aqueous activity can be local and sourced from the subsurface (37), widespread shifts in wind-drag ripple size can indicate global changes in atmospheric density, and should prove an important geological indicator of the drying of Mars (figs. S8 and S9).

#### REFERENCES AND NOTES

1. G. V. Middleton, J. B. Southard, *Mechanics of Sediment Movement* (SEPM Society for Sedimentary Geology, Tulsa, OK, ed. 2, 1984).
2. J. Grotzinger, A. Hayes, M. Lamb, S. McLennan, in *Comparative Climatology of Terrestrial Planets*, S. Mackwell, M. Bullock, J. Harder, Eds. (Univ. of Arizona Press, 2013), pp. 439–472.
3. N. Thomas et al., *Science* **347**, aaa0440 (2015).
4. I. G. Wilson, *Sedimentology* **19**, 173–210 (1972).
5. D. Rubin, D. McCulloch, *Sediment. Geol.* **26**, 207–231 (1980).
6. J. F. Kok, E. J. Parteli, T. I. Michaels, D. B. Karam, *Rep. Prog. Phys.* **75**, 106901 (2012).
7. Materials and methods are available as supplementary materials on Science Online.
8. N. T. Bridges et al., *Geology* **40**, 31–34 (2011).
9. N. Bridges et al., *Geophys. Res. Lett.* **34**, L23205 (2007).
10. A. S. McEwen et al., *J. Geophys. Res. Planets* **112**, E05S02 (2007).
11. R. Sullivan et al., *Nature* **436**, 58–61 (2005).
12. D. J. Jerolmack, D. Mohrig, J. P. Grotzinger, D. A. Fike, W. A. Watters, *J. Geophys. Res. Planets* **111**, E12S02 (2006).
13. D. F. Blake et al., MSL Science Team, *Science* **341**, 1239505 (2013).
14. J. P. Grotzinger et al., *Space Sci. Rev.* **170**, 5 (2012).
15. S. Silvestro et al., *Geology* **41**, 483–486 (2013).
16. D. M. Rubin, *Earth Sci. Rev.* **113**, 176–185 (2012).
17. B. Werner, P. Haff, R. Livi, R. Anderson, *Geology* **14**, 743 (1986).
18. H. Yizhaq, J. Kok, I. Katra, *Icarus* **230**, 143–150 (2014).
19. O. Durán, P. Claudin, B. Andreotti, *Proc. Natl. Acad. Sci. U.S.A.* **111**, 15665–15668 (2014).
20. B. Andreotti, P. Claudin, O. Pouliquen, *Phys. Rev. Lett.* **96**, 028001 (2006).
21. S. de Silva, M. Spagnuolo, N. Bridges, J. Zimbleman, *Geol. Soc. Am. Bull.* **125**, 1912–1929 (2013).
22. J. B. Southard, L. A. Boguchwal, *J. Sediment. Res.* **60**, 658–679 (1990).
23. R. Bagnold, *The Physics of Blown Sand and Desert Dunes* (Methuen and Co., London, 1941), vol. 10.
24. R. A. Grazer, *Experimental Study of Current Ripples Using Medium Silt* (Massachusetts Institute of Technology, 1982).
25. M. S. Yalin, *J. Hydraul. Eng.* **111**, 1148–1155 (1985).

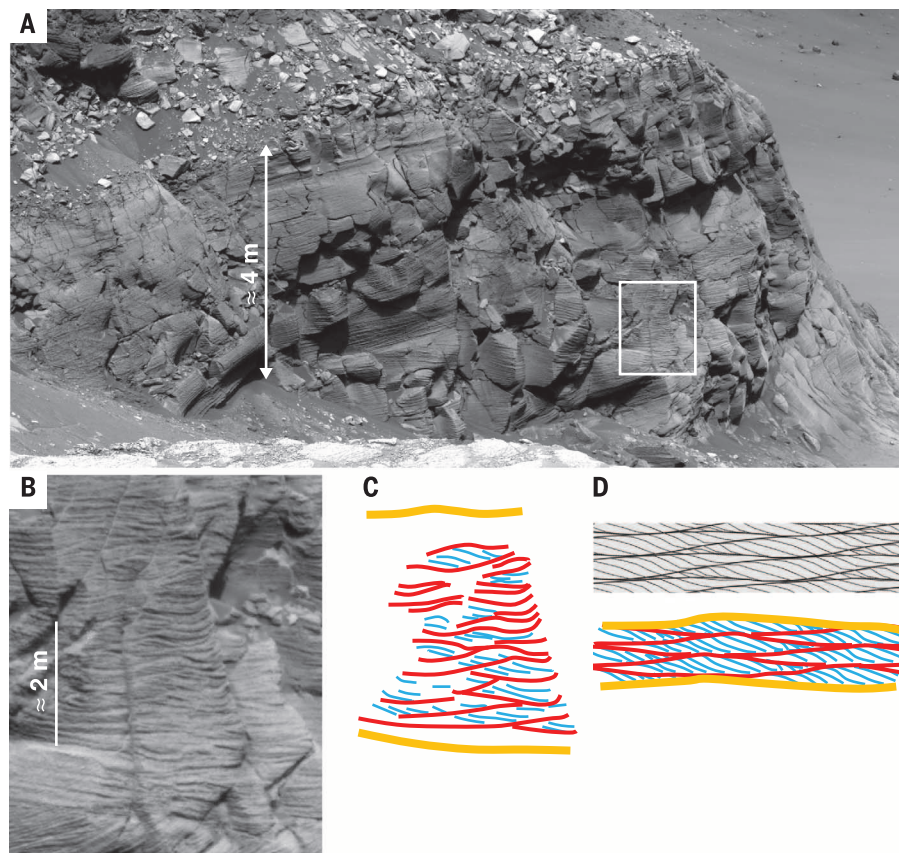


**Fig. 4. Candidate wind-drag ripple stratification on Mars.** (A) Mars Exploration Rover Panoramic Camera (39) image (P2441, sol 1212) of Cape St. Mary outcrop, Victoria crater, Mars. The white box shows the location of (B) decimeter-scale trough cross-strata and (C) an interpretation of stratal features from (B). (D) Uninterpreted (top) and interpreted (bottom) stratification produced by kinematic modeling of compound bedforms (29). Yellow lines represent surfaces scoured by dune troughs, red lines represent erosional surfaces produced by the migration of wind-drag ripples, and blue lines indicate wind-drag ripple cross-stratification.

26. M. P. Lamb, J. P. Grotzinger, J. B. Southard, N. J. Tosca, *Sedimentary Geol. Mars* **102**, 139 (2012).
27. J. P. Grotzinger *et al.*, *Earth Planet. Sci. Lett.* **240**, 11–72 (2005).
28. R. Hu, D. M. Kass, B. L. Ehlmann, Y. L. Yung, *Nat. Commun.* **6**, 10003 (2015).
29. D. M. Rubin, C. L. Carter, *Bedforms 4.0: MATLAB Code for Simulating Bedforms and Cross-Bedding* (Open-File Report 2005-1272 of the U.S. Geological Survey, 2005).
30. P. Withers, M. D. Smith, *Icarus* **185**, 133–142 (2006).
31. R. E. Hunter, *Sedimentology* **24**, 361–387 (1977).
32. A. Hayes *et al.*, *J. Geophys. Res. Planets* **116**, E00F21 (2011).
33. R. Arvidson *et al.*, *J. Geophys. Res. Planets* **111**, E02S01 (2006).
34. N. J. Tosca *et al.*, *Earth Planet. Sci. Lett.* **240**, 122–148 (2005).
35. N. J. Tosca, S. M. McLennan, M. P. Lamb, J. P. Grotzinger, *J. Geophys. Res. Planets* **116**, E05004 (2011).
36. P. R. Mahaffy *et al.*, *Science* **347**, 412–414 (2015).
37. L. Ojha *et al.*, *Nat. Geosci.* **8**, 829–832 (2015).
38. R. D. Lorenz, N. T. Bridges, A. A. Rosenthal, E. Donkor, *Icarus* **230**, 77–80 (2014).
39. J. Bell III *et al.*, *J. Geophys. Res. Planets* **108**, E12, 8063 (2003).

## ACKNOWLEDGMENTS

We thank the MSL engineering and science teams; the Mastcam team; Malin Space Science Systems, who made the rover observations possible; and B. Ehlmann and K. Edgett for insightful comments. Data presented in this paper are archived in the Planetary Data System (<https://pds.nasa.gov/>), and our compilation is available in the supplementary materials (data tables S1 and S2). Part of this research was carried out at the Jet

Propulsion Laboratory—Caltech, under a contract with NASA. Work in the United Kingdom was funded by the UK Space Agency. D.M.R. was funded by the NASA MSL Participating Scientist program, and A.A.F. by a KISS Prize Postdoctoral Fellowship and a Caltech GPS Division Texaco Prize Postdoctoral Fellowship.

## SUPPLEMENTARY MATERIALS

[www.sciencemag.org/content/353/6294/55/suppl/DC1](http://www.sciencemag.org/content/353/6294/55/suppl/DC1)

Materials and Methods

Supplementary Text

Figs. S1 to S10

Tables S1 to S3

References (40–89)

Data Tables S1 and S2

25 January 2016; accepted 31 May 2016

10.1126/science.aaf3206

## SOLAR CELLS

# A vacuum flash–assisted solution process for high-efficiency large-area perovskite solar cells

Xiong Li,<sup>1\*</sup> Dongqin Bi,<sup>2\*</sup> Chenyi Yi,<sup>1\*</sup> Jean-David Décoppet,<sup>1</sup> Jingshan Luo,<sup>1</sup> Shaik Mohammed Zakeeruddin,<sup>1</sup> Anders Hagfeldt,<sup>2</sup> Michael Grätzel<sup>1†</sup>

Metal halide perovskite solar cells (PSCs) currently attract enormous research interest because of their high solar-to-electric power conversion efficiency (PCE) and low fabrication costs, but their practical development is hampered by difficulties in achieving high performance with large-size devices. We devised a simple vacuum flash–assisted solution processing method to obtain shiny, smooth, crystalline perovskite films of high electronic quality over large areas. This enabled us to fabricate solar cells with an aperture area exceeding 1 square centimeter, a maximum efficiency of 20.5%, and a certified PCE of 19.6%. By contrast, the best certified PCE to date is 15.6% for PSCs of similar size. We demonstrate that the reproducibility of the method is excellent and that the cells show virtually no hysteresis. Our approach enables the realization of highly efficient large-area PSCs for practical deployment.

In the span of a few years, the power conversion efficiency (PCE) of perovskite solar cells (PSCs) has risen from 3.8% (1) to 22.10% (2), which is unprecedented in the field of photovoltaics. However, such high efficiencies have been achieved only with cells of very small size—between 0.04 and 0.2 cm<sup>2</sup>—and few investigators have attempted to fabricate larger-area cells (3–10). The use of small-area devices has raised some doubts on the remarkable progress of the PSC field because the measurement errors tend to increase as the active cell area becomes smaller. Thus, the development of PSCs with a mandatory minimum active area of >1 cm<sup>2</sup> is required for the evaluation of this new photovoltaic (PV) technology (3, 8). At present, the best certified PCE of a cell with a size exceeding the critical threshold

of 1 cm<sup>2</sup> is 15.6% (11) because of the limitations of current preparation methods (12–15). Top-performing PSCs often are made with an antisolvent such as chlorobenzene to precipitate the perovskite or its intermediate from its solution, which typically contains a solvent mixture of  $\gamma$ -butyrolactone (GBL), dimethylformamide (DMF), and dimethylsulfoxide (DMSO) (3, 7, 8, 14, 16–19). The antisolvent induces oversaturation of the perovskite solution, but because the antisolvent is usually dripped in the center of the film during spin-coating, the result is a radial gradient in oversaturation; the spatially inhomogeneous nucleation of the perovskite or its intermediate ultimately leads to defects in the perovskite film (3, 20). In addition, the antisolvents currently used are toxic and harmful to the environment, hampering their large-scale application (8, 14). Thus, alternative procedures for preparing large-area PSCs are warranted if their performance on a large device area is to be competitive with that of inorganic thin-film photovoltaics.

We developed a simple and effective method to produce high-quality perovskite films for large-

area PSCs by applying a vacuum-flash treatment during the solution processing of the perovskite. Our approach differs from previous studies that used high-vacuum methods for vapor deposition of the perovskite (13, 15) or for removal of reaction products (i.e., methylammonium chloride) by sublimation during the thermal annealing of the films (21). Vacuum flash–assisted solution processing (VASP) is a method that enables the sudden and well-controlled removal of solvent, thereby boosting rapid crystallization of a fibrous material that consists of a Lewis acid-base-type adduct representing the perovskite precursor phase (19). Upon thermal annealing, the precursor phase produces highly oriented, crystalline perovskite films of excellent electronic quality that can be grown on a variety of substrates (17–19). Furthermore, VASP allows deposition of the perovskite films on large substrate sizes and can be turned into a continuous process.

We achieved a maximum PCE of 20.5% and a certified PCE of 19.6% for large cells with square aperture areas greater than 1 cm<sup>2</sup>, which is commensurate with the 21.0% reached by today's best thin-film copper indium gallium selenide (CIGS) and CdTe devices of similar size (11). Our method also eliminates the hysteresis in the current-voltage ( $J$ - $V$ ) curves, a notorious problem with PSCs (22). We tested the method with state-of-the-art perovskites using formamidinium (FA) and methylammonium (MA) mixed-cation and iodide-bromide mixed-anion perovskite formulations (16, 23) of composition FA<sub>0.81</sub>MA<sub>0.15</sub>PbI<sub>2.51</sub>Br<sub>0.45</sub>. To demonstrate the versatility of the method, we also prepared the emerging cesium (Cs<sup>+</sup>) and FA mixed-cation perovskite FA<sub>0.9</sub>Cs<sub>1-x</sub>PbI<sub>y</sub>Br<sub>3-y</sub> formulations (24–26). The VASP method is also readily scalable to the industrial level.

The basic steps of perovskite film fabrication by the VASP method are shown in Fig. 1A. The perovskite precursor solution, of composition FA<sub>0.81</sub>MA<sub>0.15</sub>PbI<sub>2.51</sub>Br<sub>0.45</sub> containing DMSO with a nominal 1:1 ratio of lead to DMSO, was first spin-coated on top of a mesoporous TiO<sub>2</sub> film prepared as described (16). The film was then placed for a few seconds into a vacuum chamber to boost rapid crystallization of the perovskite intermediate phase by removing most of the residual solvents, consisting mainly of GBL and DMF. We observed that the pressure applied

<sup>1</sup>Laboratory of Photonics and Interfaces, Department of Chemistry and Chemical Engineering, École Polytechnique Fédérale de Lausanne, Lausanne CH-1015, Switzerland.

<sup>2</sup>Laboratory of Photomolecular Science, Department of Chemistry and Chemical Engineering, École Polytechnique Fédérale de Lausanne, Lausanne CH-1015, Switzerland.

\*These authors contributed equally to this work. †Corresponding author. Email: [michael.gratzel@epfl.ch](mailto:michael.gratzel@epfl.ch)